78. C. S. Kochanek, *ibid.* **453**, 545 (1995); *ibid.* **466**, 638 (1996).
79. E. E. Falco, C. S. Kochanek, J. A. Munoz, *ibid.* **494**, 47 (1998).
80. J. Wambsganss, R. Cen, J. P. Ostriker, E. L. Turner, *Science* **268**, 274 (1995); *Astrophys. J.*, in press (available at http://xxx.lanl.gov/abs/astro-ph/9610096).
81. M. Bartelmann *et al.*, *Astron. Astrophys.* **330**, 1 (1998).
82. For an introduction to the CMB power spectrum and its interpretation see P. J. Steinhardt, in *Particle and Nuclear Astrophysics and Cosmology in the Next Millenium*, E. W. Kolb and P. Peccei, Eds. (World Scientific, Singapore, 1995), pp. 51–72.
83. The physics of CMB anisotropy generation is discussed in W. Hu, N. Sugiyama, J. Silk, *Nature* **386**, 37 (1997).
84. M. Kamionkowski, D. N. Spergel, N. Sugiyama, *Astrophys. J.* **426**, L57 (1994).
85. G. F. Smoot *et al.*, *ibid.* **396**, L1 (1992); C. L. Bennett *et al.*, *ibid.* **464**, L1 (1996).
86. M. J. Devlin *et al.*, *ibid.* **509**, L69 (1998); T. Herbig *et al.*, *ibid.*, p. L73; A. Oliveira-Costa *et al.*, *ibid.*, p. L77.
87. S. R. Platt *et al.*, *ibid.* **475**, L1 (1997).
88. E. S. Cheng *et al.*, *ibid.* **488**, L59 (1997).
89. B. Netterfield, M. J. Devlin, N. Jarosik, L. Page, E. L. Wallack, *ibid.* **474**, 47 (1997).
90. P. F. Scott, *et al.*, *ibid.* **461**, L1 (1996).
91. E. M. Leitch, A. C. S. Readhead, T. J. Pearson, S. T. Myers, S. Gulkis, *ibid.*, in press (available at http://xxx.lanl.gov/abs/astro-ph/9807312).
92. G. Jungman, M. Kamionkowski, A. Kosowsky, D. Spergel, *Phys. Rev. D* **54**, 1332 (1996).
93. For the current status of parameter estimation from CMB data, see J. R. Bond and A. H. Jaffe, available at http://xxx.lanl.gov/abs/astro-ph/9809043.
94. R. L. Davis, H. M. Hodges, G. F. Smoot, P. J. Steinhardt, M. S. Turner, *Phys. Rev. Lett.* **69**, 1856 (1992).
95. U. Seljak and M. Zaldarriaga, *ibid.* **78**, 2054 (1997); *Phys. Rev. D* **55**, 1830 (1997).
96. M. Kamionkowski, A. Kosowsky, A. Stebbins, *Phys. Rev. Lett.* **78**, 2058 (1997); *Phys. Rev. D* **55**, 7368 (1997).
97. B. Sadoulet, *Rev. Mod. Phys.* **71S**, 197 (1999).
98. L. J. Rosenberg, *Proc. Natl. Acad. Sci. U.S.A.* **95**, 59 (1998).
99. G. Jungman, M. Kamionkowski, K. Griest, *Phys. Rep.* **267**, 195 (1996).
100. Y. Fukuda *et al.*, Super-Kamionkande Collaboration, *Phys. Rev. Lett.* **81**, 1562 (1998).
101. P. J. Steinhardt, L. Wang, I. Zlatev, available at http://xxx.lanl.gov/abs/astro-ph/9812313; I. Zlatev, L. Wang, P. J. Steinhardt, available at http://xxx.lanl.gov/abs/astro-ph/9807002.
102. We thank R. Caldwell, R. Cen, X. Fan, G. Huey, P. J. E. Peebles, L. Wang, and members of the SCP team for their contributions and collaborations on work described here. Supported by NSF grant AST93-15368 (N.A.B., Princeton); U.S. Department of Energy (DOE) grant DE-FG02-91ER40671 (P.J.S., Princeton); the Physics Division, E. O. Lawrence Berkeley National Laboratory of the U.S. DOE under contract DE-AC03-76SF000098; and the NSF's Center for Particle Astrophysics, University of California, Berkeley, under grant ADT-88909616 (S.P.).

REVIEW: EXPERIMENTAL ASTROPHYSICS

Modeling Astrophysical Phenomena in the Laboratory with Intense Lasers

Bruce A. Remington,[1] David Arnett,[2] R. Paul Drake,[3] Hideaki Takabe[4]

Astrophysical research has traditionally been divided into observations and theoretical modeling or a combination of both. A component sometimes missing has been the ability to quantitatively test the observations and models in an experimental setting where the initial and final states are well characterized. Intense lasers are now being used to recreate aspects of astrophysical phenomena in the laboratory, allowing the creation of experimental test beds where observations and models can be quantitatively compared with laboratory data. Experiments are under development at intense laser facilities to test and refine our understanding of phenomena such as supernovae, supernova remnants, gamma-ray bursts, and giant planets.

Modern intense lasers produce energy densities in submillimeter-scale volumes that are far larger than those produced by any other method. With these highly versatile laser facilities, matter can be prepared reproducibly in conditions that are equivalent, in a rigorously scaled sense, to those in large astrophysical systems such as supernovae, Herbig-Haro jets, or giant planets. Examples of areas that can be studied include strong shock phenomena, high–Mach number jets, strongly coupled plasmas, compressible hydrodynamic instabilities, radiation flow, photoevaporation front hydrodynamics, and fundamental properties such as opacities and equations of state (EOS).

Nuclear fusion reactions are the fundamental energy source of stars, and their cross sections quantify the individual reaction probabilities, allowing the heat production inside stars to be calculated. Opacities are the fundamental atomic properties that govern radiation transport within stars. Opacities quantify the probability that an atom will absorb photons that pass within its vicinity and consequently control to a large extent the temperature profiles of the interiors of stars. These fundamental "input" quantities—cross sections and opacities—are required in models of phenomena such as stellar pulsations and supernova light curves. The research reviewed here is aimed at probing astrophysical dynamics directly—the "output" of the models—by creating scaled reproductions of the astrophysical systems in the laboratory.

[1]Lawrence Livermore National Laboratory, L021, Livermore, CA, 94550, USA. E-mail: remington2@llnl.gov [2]Steward Observatory, University of Arizona, Tucson, AZ, 85721, USA. E-mail: darnett@as.arizona.edu [3]Atmospheric, Oceanic, and Space Sciences, University of Michigan, 2455 Hayward Street, Ann Arbor, MI, 48109–2143, USA. E-mail: rpdrake@umich.edu [4]Institute of Laser Engineering, Osaka University, Yamada-Oka 2-6, Shita, Osaka 565, Japan. E-mail:takabe@ile.asaka-u.ac.jp

Supernovae

Core-collapse supernovae (SNe) represent the dramatic endpoint in the life cycle of a star (*1*–*5*). The final death throes of the star are spent in a high-stakes "tug of war" pitting quantum mechanical degeneracy pressure against gravitational pressure. The outcome determines whether the final state is a white dwarf, neutron star, or black hole and is based on the strength of the degeneracy pressure to withstand the radially inward tug of gravity (*6*). Stars with initial masses of 1 to 8 $M_\odot$ (where $M_\odot$ corresponds to the mass of the sun) finish their hydrogen burning while their cores are not yet degenerate. They undergo core contraction, which raises the core density and temperature sufficiently to trigger He burning. These stars subsequently lose mass effectively and end their lifetimes as white dwarfs, with masses of $\sim$0.6 $M_\odot$. White dwarfs are supported by the pressure of the degenerate electrons in their interiors; that is, it is the quantum mechanical Pauli exclusion principle that prevents further collapse. The maximum mass possible for a white dwarf is the Chandrashekar limiting mass, $M_{Ch} \approx 1.4\ M_\odot$. More massive stars have high enough temperatures in their cores to continue the nuclear fusion burning cycle up to Fe. Once the core reaches Fe, the nuclear fusion reactions no longer release net energy (because the nuclear binding energy per nucleon is maximum in Fe, at nearly 9 MeV per nucleon), and the thermonuclear fires are extinguished. The mass of the Fe core continues to grow as the surrounding layers burn their way to this thermonuclear end point until the Fe core mass

exceeds ~1.4 $M_\odot$. At this point, there is no longer sufficient heat produced in the core to balance cooling by neutrino emission and photonuclear dissociation, and the core surrenders to gravity, triggering a catastrophic gravitational collapse that is over in a matter of seconds. This collapse is arrested only when the core density reaches that of degenerate nuclear matter (~2×10^{14} g/cm^3). The Fermi degeneracy pressure, $p_{deg} \sim \rho^{2/3}$ (where ρ is density), increases sufficiently to stop the implosion, and a spectacular nuclear rebound occurs whose strength is determined by the EOS of bulk nuclear matter. By a mechanism still debated, this launches the powerful outward-propagating shock wave (SW) that first "stalls" in the infalling matter and then gets reenergized by convection and by energy deposition due to neutrinos emitted from the core. Thus restarted, the SW traverses the overlying layers and effectively blows the star apart. Thus, the catastrophic end of the massive star marks the spectacular beginning of a core-collapse supernova (SN). This explosive birth is observed as a bright flash of ultraviolet (UV) light (*3*, *7*). If the core has a mass larger than 2 to 3 $M_\odot$, the core collapse continues to form a black hole.

The visual SN commences when the SW breaks out through the surface of the star about an hour after the core collapses (*3*). There is a sudden increase in temperature to 20 to 30 eV and luminosity, followed by a rapid drop in both quantities, as the star expands and cools adiabatically. About 30 min after SW breakout, the luminosity approaches a constant value, as the recombination front, which determines the photosphere, moves inward in mass at a constant temperature (for hydrogen) of about 6000 K. After some 20 to 40 days, the heat from the radioactive core, heated by Compton scattering of the γ-rays produced from ^{56}Ni, ^{56}Co, and ^{44}Ti, reaches the photosphere, and the light curve rises up in a broad secondary maximum. Subsequently, the decay of the light curve is monotonic in time at a rate determined by the half-lives of the various radioactive nuclei that serve as the heat source. The light curve contains a wealth of information about the star and its explosion. The luminosity varies directly with the explosion energy per unit mass, E/M, and is also proportional to the initial radius of the star. For the same E/M, SNe from small stars are not as bright, because more energy goes into hydrodynamic expansion. The luminosity is on average inversely proportional to the opacity, because lower opacity means shorter radiative diffusion times. Finally, the light curve time evolution is sensitive to the degree that the core hydrodynamically mixes outward into the envelope, bringing heat nearer to the photosphere. The ability to quantitatively calculate an SN light curve would allow the intrinsic brightness of the SN to be determined. Comparison with the observed brightness would give its distance, through the expanding photosphere method (*8*, *9*). Together with spectroscopic measurements of its redshift, this allows the Hubble constant H_0 to be determined (*10*). There are several aspects to synthetic light curve calculations that could benefit from laboratory experiments, such as radiation flow, opacities, and hydrodynamic mixing.

Exploding stars create a homologous expansion, where each radiating region resides in a velocity gradient and sees plasma receding from it in all directions. For photons emitted in one region to escape the star, they have to pass through "windows" in opacity, where the absorption probability is low. In other words, the absorbing regions are always redshifted relative to the emitting regions. To be able to construct a synthetic light curve requires that one calculate these "expansion opacities." Such calculations are complex, and sophisticated opacity codes such as OPAL (*11*) are indispensable.

Experiments are being developed to test these difficult opacity calculations, focusing on atomic transitions that have not been explored. For example, in one experiment, a 25-nm-thick iron foil was sandwiched between two C layers and heated to ~20 eV with x-rays. The absorption spectrum near 730 eV was measured and analyzed, comparing several different opacity calculations (*12*). In another experiment, radiation line transport was measured in an expanding plasma (*13*). This experiment studied the structure of a doublet in the aluminum spectrum, at a wavelength near 7.18 Å. The emission occurs from an optically thick plasma with a substantial velocity gradient, so that emission in one line is often absorbed and reemitted by the other line at another location in the plasma. The resulting line structure is complex but can be reproduced by modeling only when this expansion effect on the radiation transport is taken into account. Hence, experiments are under development to test opacity calculations, both static and in expansion, relevant to SN light curves.

A core-collapse SN is driven by a powerful SW, and strong SWs are the breeding ground of hydrodynamic instabilities. Two such instabilities seem particularly important: the Rayleigh-Taylor (RT) and Richtmyer-Meshkov (RM) instabilities. The RT instability occurs when effective gravity (due to acceleration) tries to pull a heavier fluid through an underlying lighter one (for example, large air bubbles under water or heated gas from a powerful explosion in the atmosphere). The RM instability is closely related, with the role of gravity replaced by the inertia from an impulsive acceleration due to an SW.

During the SW transit phase, the RM instability is triggered at each discontinuity in the density profile of the star, that is, at the O-He and He-H "interfaces." After SW transit, hydrodynamic mixing continues because of the RT instability, as the denser layers are decelerated by the lower density outer layers. The outward mixing of the higher density, radioactive core material (for example, ^{56}Ni, ^{56}Co, and ^{44}Ti) brings the radioactive heat source toward the surface of the star. These explosion products decay by the emission of γ-rays, which Compton scatter off electrons in their vicinity. The consequent reheating of the photosphere causes the secondary maximum in the light curve. The RT mixing induces this reinvigoration of the light curve to start earlier, broadening the secondary maximum. Observations of the light curve of SN1987A unambiguously showed this broadening of the secondary peak, suggesting enhanced transport from the core out to the photosphere (*1*, *2*). Two-dimensional calculations of the development of the mixing at the O-He and He-H interfaces with the SN code PROMETHEUS (*14*, *15*) show that spikes of denser oxygen and helium penetrate outward into the less dense envelope of hydrogen, whereas bubbles of hydrogen move inward relative to the average location of the H/He boundary (Fig. 1A). This interpenetration occurs through the growth and nonlinear

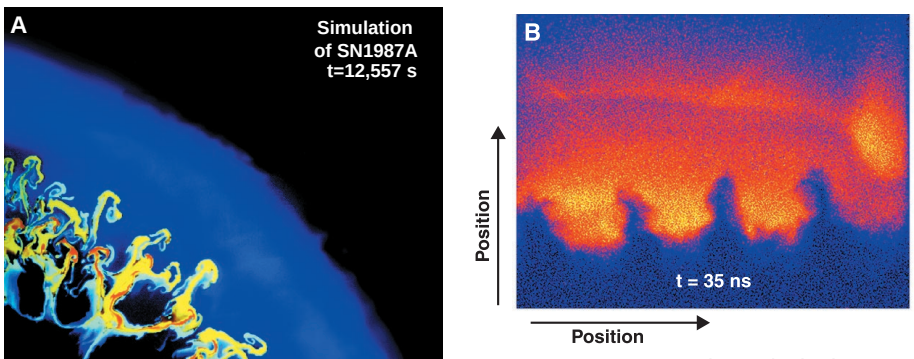

Fig. 1. Mixing in SN explosion hydrodynamics. (**A**) Image of simulated hydrodynamic mixing from SN1987A at t = 12,557 s [reproduced with permission from (*14*)]. (**B**) An image from a laser experiment designed to measure this hydrodynamic mixing of a λ = 200 μm ripple under scaled conditions at t = 35 ns [reproduced from (*53*)].

evolution of the RT instability.

Laser-based experiments can generate strong-SW–initiated nonlinear hydrodynamic mixing conditions similar to those found in SNe. In a set of experiments scaled to reproduce the hydrodynamics of the He-H interface of SN1987A about an hour after explosion, a strong SW was passed through an interface separating dense "core" material (Cu) from the lower density outer envelope (CH_2) (*16*, *17*). A two-dimensional (2D) sinusoidal ripple (1D wave vector) was imposed at the interface. The subsequent 2D growth due to the RM and RT instabilities was measured by x-ray backlighting. Spikes of Cu penetrating upward into less dense CH_2 were observed as a consequence of the RT instability (Fig. 1B). This interpenetration was calculated in 2D with PROMETHEUS, and the simulations reproduced the observations.

A theoretical look at the relation between the hydrodynamics occurring in the SN compared with that in the laboratory experiment shows that a rigorous mapping exists. Consider the He-H interface at 1600 s in the SN and the Cu-CH interface at 20 ns in the laser experiment. In both settings, the Reynold's number (the ratio of the inertial to the viscous force) and the Peclet number (the ratio of the convective to the conductive heat transport) are large. Therefore, viscosity and thermal diffusivity are negligible, and the dynamics of the interface are well described by Euler's equations for a polytropic gas (*18*):

$$\rho\left(\frac{\partial \mathbf{v}}{\partial t} + \mathbf{v}\cdot\nabla\mathbf{v}\right) = -\nabla p \qquad (1a)$$

$$\frac{\partial \rho}{\partial t} + \nabla\cdot(\rho\mathbf{v}) = 0 \qquad (1b)$$

$$\frac{\partial p}{\partial t} - \gamma_a \frac{p}{\rho}\frac{\partial \rho}{\partial t} + \mathbf{v}\cdot\nabla p - \gamma_a \frac{p}{\rho}\mathbf{v}\cdot\nabla\rho = 0 \qquad (1c)$$

where ρ is density, $\mathbf{v}$ is fluid velocity, t is time, p is pressure, and γ_a is the adiabatic index. These equations represent conservation of momentum, mass, and energy, respectively. It is straightforward to show by substitution that Eq. 1 is invariant under the following scale transformation,

$$h_{SN} \rightarrow a h_{lab} \qquad (2a)$$

$$\rho_{SN} \rightarrow b \rho_{lab} \qquad (2b)$$

$$p_{SN} \rightarrow c p_{lab} \qquad (2c)$$

$$\tau_{SN} \rightarrow a(b/c)^{1/2}\tau_{lab} \qquad (2d)$$

where h, ρ, p, and τ correspond to characteristic spatial, density, pressure, and time scales and subscripts SN and lab refer to calculations of the SN and laboratory laser experiment, respectively. When transformation 2 is inserted into Eq. 1, the constants a, b, and c cancel, and the dynamics described by Euler's equation are indistinguishable in the SN and the laser experiment. Any insights gained through the laser experiment apply directly to the SN through the mapping described by Eq. 2. For example, the hydrodynamics illustrated in Fig. 1, A and B, are similar and can be related through the SN-to-laboratory mapping of h, ρ, p, τ, and acceleration $g = \nabla p/\rho$ (Eq. 2) giving 10^{11} cm to 50 μm, 8×10^{-3} g/cm^3 to 4 g/cm^3, 40 Mbar to 0.6 Mbar, and $10g_o$ to $10^{10}g_o$, where g_o corresponds to the acceleration due to gravity at the surface of Earth. These values were taken at times of 2000 s for the SN and 20 ns for the laboratory experiment (*18*).

Supernova Remnants

Although SN explosions mark the end of massive stars, they also mark the beginning of their new lives as supernova remnants (SNRs). Well-known examples of SNRs such as the remnants of Tycho's SN (*19*), Kepler's SN (*20*), the Cygnus loop (*21*), SN1006 (*22*), and the Crab nebula (*23*) provide exquisite visual testimony to their violent births. There are several active areas of research regarding the dynamics and evolution of SNRs that may be better understood with laser experiments.

SW dynamics dominate the evolution of SNRs. The rapidly expanding ejecta from the SN drive an SW forward into the surrounding medium, and a reverse SW forms where the ejecta are decelerated by the accumulating, shocked matter. The place where the ejecta and ambient medium meet, called the contact discontinuity, becomes hydrodynamically unstable. Currently, the most actively observed SNR is the young remnant forming around SN1987A. This remnant consists of the standard SN ejecta expanding into the ambient medium, as well as a mysterious inner and two outer circumstellar nebular rings, which apparently existed before the SN explosion. Various models have been proposed for these rings, but as of yet no explanation fully explains their origin. The SN ejecta, however, are moving very fast (~10^4 km/s) compared with the nearly static (~10 km/s) inner ring, which has a diameter of ~1 light-year. It is expected that the ejecta-forward SW system will impact the inner edge of the inner ring within the next ~5 years. This impact should launch a strong SW into the ring, heating it to 100- to 300-eV temperatures, and cause emissions at wavelengths from optical to x-ray. Observation of this impact should shed light on the structure, composition, and hopefully origin of the rings. Recent images of the inner ring (*24*–*26*) show a rapidly brightening, localized hot spot (upper right corner of Fig. 2A), suggesting that perhaps the collision of the forward SW with the ring has actually started. Spectral imaging of Lyman-α radiation, which is produced at the reverse SW, indicates that the reverse SW has traversed about 80% of the distance from the ring to the star (*24*).

Laser experiments can produce SW structures similar to those in a SNR, under well-scaled hydrodynamic conditions (*18*, *27*–*29*). Experiments have been developed in 1D to reproduce the basic dynamics of SNR formation: fast moving SW-induced ejecta sweeping into a surrounding low-density, static ambient atmosphere. This launches a forward SW into the ambient medium and a reverse SW into the stagnating ejecta (Fig. 2B), much like the dynamics of SNR formation. Indeed, the laboratory experiment can be modeled by the self-similar model of Chevalier (*30*) developed to describe the 1D dynamics of SNRs.

Expectations are that the contact discontinuity (the meeting point of the ejecta and ambient plasmas) will be hydrodynamically unstable, and 2D experiments have begun to look at this. One of the driving motivations for studying SNR physics relevant to SN1987A is the long-awaited impact of the SN blast wave with the inner circumstellar

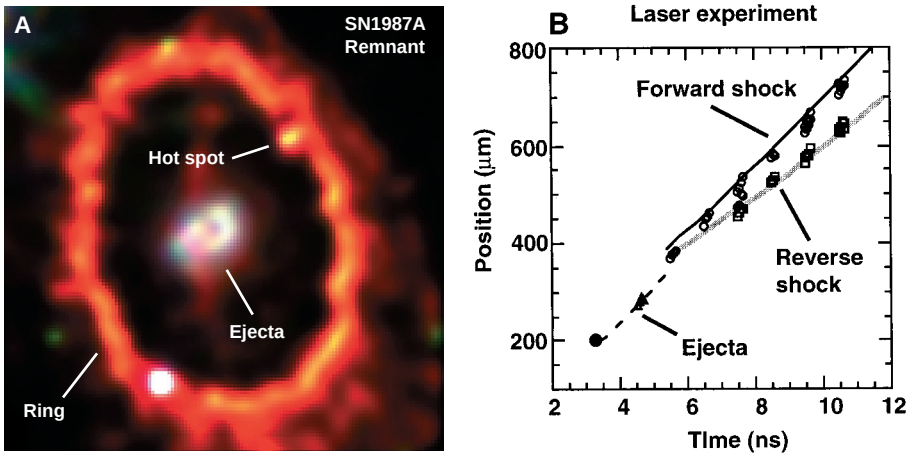

Fig. 2. Young SN remnant dynamics. (**A**) Observational image of the inner circumstellar ring of SN1987A (http://antwrp.gsfc.nasa.gov/apod/ap980217.html) (image courtesy of the Supernova Intensive Study Team; PI: Robert Kirshner). (**B**) Image from SW experiments designed to produce similar, scaled regimes of strong SW hydrodynamics [reproduced with permission from (*28*)].

nebular ring. The interaction of the SW with the ring is sure to be rich in 3D strong SW effects. A laser experiment is being developed to elucidate the 3D nature of the interaction of a strong SW with a localized high-density feature such as a sphere (*31*). The 3D development strongly affects the interactions, with azimuthal (3D) modes growing and enhancing the "shredding" of the sphere. A similar 3D effect is likely for the interaction of the SN1987A blast wave with the inner ring and in SW-cloud interactions in general (*32*).

Under the current conditions for the remnant of SN1987A, the scale transformation based on Euler's equations described above for the explosion hydrodynamics might be applied again. For this to be relevant, one has to consider whether the SW is radiative and whether the ambient magnetic field localizes the plasma. For the current conditions of SN1987A, the plasma density is low enough that the SWs are not radiative; that is, the radiative cooling time scale (τ_{rad}) is long compared with a hydrodynamic time scale (τ_{hydro}): $\tau_{rad}/\tau_{hydro} \gg 1$. Also, the ambient magnetic field, $B = \sim 100$ μG, is large enough that the ion Larmor radius is much smaller than spatial scales of interest. Hence, the plasma can be treated hydrodynamically, the dynamics can be treated again with Euler's equations (Eq. 1), and the same rigorous scale transformation (Eq. 2) holds. For the SNR-to-laboratory transformation corresponding to the 1D experiment shown in Fig. 2B, we get 0.03 light-year mapping to 100 μm, 10^4 km/s to 60 km/s, and 1 year mapping to 1 ns (*18*), where these values correspond to times of 13 years in the SNR and 8 ns in the laboratory experiment.

Spectral analysis of SW-induced astrophysical emissions can yield the temperature, density, degree of equilibration, ionization state, and velocity of the SW. With an additional measure of the proper motion of the SW, the distance to the emitting source can also be determined. Such analysis of the SW-induced emissions of hydrogen (Lyman β) and ionized oxygen (O VI) from the remnant of SN1006, which exploded in the year 1006 at a distance of 2 kpc (*22*), shows that the plasma behind the SW front is not cooling rapidly by radiation: $\tau_{rad}/\tau_{hydro} \gg 1$. The conclusion from this spectral analysis is that plasma turbulence in the SW front is not effective in producing temperature equilibration among the different ion species.

Gamma-Ray Bursts

Gamma-ray bursts (GRBs) are the greatest enigma in contemporary astrophysics (*33–37*). Detected at a rate of more than one per day from random directions in the sky, GRBs typically have burst durations of a few seconds, at photon energies of 0.1 to 10 MeV (Fig. 3A). GRB distances remained unknown for the past two decades, primarily because their radiation in all wavelengths other than γ-rays was undetected. This changed recently with the determination of accurate positions (to within about 3 minutes of arc), obtained within hours of outburst by the BeppoSAX satellite. Optical spectroscopy of the light associated with the outburst, the "afterglow," established that at least some of the GRBs are at cosmological distances of several billion light-years (redshifts of $\Delta\lambda/\lambda = 1$ to 3). To generate the observed luminosities then requires total source energies of $\sim 10^{53}$ ergs per burst. The rapid rise time and rapid variability, $\Delta t \sim 1$ ms, observed in some bursts imply a source size, $R_i \sim c\Delta t \sim 10^7$ cm; that is, these tremendous total energies appear to be emitted from very compact sources. The observed photon energy spectra can extend to ~100 MeV, have a power-law shape (Fig. 3A), and are fit with a simple functional form:

$$N(E)dE \sim E^{-\alpha}dE \qquad (3)$$

where N is the photon number density at energy E, with spectral index $\alpha \sim 2$. This suggests that the source plasma is optically thin to the radiation observed. (If the source plasma were optically thick, the photons would thermalize, and the observed spectrum would have a Planckian, not a power-law shape.) This presents a problem. When two photons with energies E_1 and E_2 interact, their center-of-mass energy is $\sim 2(E_1E_2)^{1/2}$, and the interaction can produce an e^+e^- pair if $(E_1E_2)^{1/2} > m_ec^2$, where m_e represents the rest mass of an electron (*33*). Denote the fraction of photon pairs in a GRB satisfying this condition as f_p. The optical depth (OD) for the $\gamma\gamma \rightarrow e^+e^-$ process, varies as OD ~ f_p/R_i^2. Pairs are produced prodigiously, and by Compton scattering, they would make the plasma optically thick, thermalizing the photon spectrum. The observed spectra, however, are nonthermal, hence the "compactness problem." The fireball model was developed to resolve this problem without introducing "new physics." In this model, the source creates a relativistically expanding fireball so that the emission region is moving toward the observer at relativistic velocities (*33*, *36*). Consider a source of radiation moving toward an observer at rest with a relativistic velocity (V) characterized by a Lorentz factor (γ_L), $\gamma_L = 1/(1 - V^2/c^2)^{1/2} \gg 1$. The observer detects photons with energy $h\nu_{obs}$ (where h is the Planck constant and ν_{obs} is the photon frequency observed), whereas these photons in the rest frame of the emission region have energy $h\nu_{obs}/\gamma_L$. Hence, at the emitter, the fraction of photons with energies high enough to produce e^+e^- pairs, f_p, is reduced by a factor $\gamma_L^{-2\alpha}$. Also, the emitting region appears Lorentz contracted, so that in its rest frame, the emission region is larger, with $R_i \sim \gamma_L^2 c\Delta t$. The result is that the OD for the process $\gamma\gamma \rightarrow e^+e^-$ now varies as OD ~ $f_p/\gamma_L^{4+2\alpha}R_i^2$, which for $\gamma_L > \sim 100$ resolves the compactness problem. Through the blue-shift boost, we observe the high-energy photons, but the emission region remains optically thin, giving the observed γ-ray power-law spectrum. The kinetic energy of the GRB ejecta is assumed to be randomized behind internal ("reverse") SWs and emitted as high-energy photons when the SW is at a radius of $r_{int} = \gamma_L^2 c\Delta t = 10^{12}$ to 10^{13} cm, for $\gamma_L = 100$ to 300. The "afterglow" is assumed to happen from emissions behind the external ("forward") SW at a radius of $r_{ext} > \sim 10^{17}$ cm.

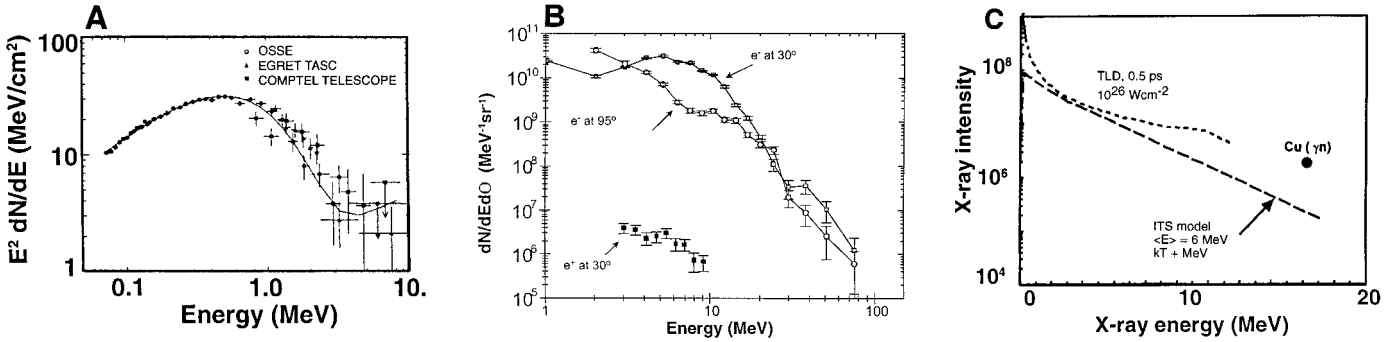

Fig. 3. GRBs and relativistic plasmas. (**A**) Experimental γ-ray energy spectrum from GRB910601 [reproduced from (*34*)]. (**B**) Measured electron energy spectrum from Petawatt laser experiments (280 J, 0.45 ps, ~10^{20} W/cm² on 0.5 mm Au) [reprinted with permission from (*41*)]. (**C**) Measured x-ray energy spectrum from experiments with the Petawatt laser [reprinted with permission from (*40*), copyright 1998, American Institute of Physics].

Most GRBs show variability on time scales much shorter than (typically one-hundredth of) the total GRB duration (*35*). In the fireball model, such variability comes from internal ("reverse") SWs, which convert a substantial part of the directed kinetic energy to internal energy. This energy is then radiated as γ-rays by synchrotron and inverse-Compton emission of SW-accelerated electrons. The GRB overall duration reflects the duration over which energy is emitted from the source. After internal SWs, the fireball rapidly cools and continues to expand, driving a relativistic SW into the surrounding interstellar medium gas. This external SW continuously heats new gas and produces relativistic electrons that may produce the delayed radiation observed on time scales of days to months, that is, the afterglow. So, a relativistically expanding fireball produces the rapidly varying, hard x-rays by internal SWs and the longer lived slow "afterglow" decay by the external SW.

Despite its qualitative successes, the fireball model is incomplete. The cause of GRBs is unknown but must be spectacular because such great distances require enormous energies for the burst to appear so bright. The merger of a pair of neutron stars, the core collapse of a failed SN, and other exotic events involving black holes and relativistic jets have been suggested (*33*, *34*). Radiation escapes the fireball only after it expands to radii many orders of magnitude larger than the original source size of $\sim 10^7$ cm. The γ-ray emission occurs when the source has expanded to a radius of $\sim 10^{13}$ cm and the afterglow at $>10^{16}$ cm. Hence, the observed radiation does not provide direct information about the underlying source. The predictions of γ-ray emission from the fireball involve the interaction of plasma with SWs moving at relativistic velocities and with magnetic fields. The details of this interaction are not understood. This superheated conglomerate is thought to expand relativistically in a fiery ball or jet of plasma, with copious production of e^+e^- pairs. Explosion energies are estimated to be in the range of 10^{52} to 10^{53} ergs (approaching the rest mass energy of the sun). Monte Carlo simulations of the γ-ray spectrum of a typical GRB such as GRB0973 (*38*), with the use of a model in which energetic electrons and positrons from the fireball produce γ-rays through multiple Compton upscattering of low-energy photons, qualitatively reproduce the observed GRB spectra and time evolution. A related phenomenon is the origin of ultrahigh-energy cosmic rays (10^{20} eV), which are thought to occur by the Fermi acceleration mechanism at the fireball wave front (*35*).

In experiments under development to benchmark astrophysical codes for radiation hydrodynamics, a radiative, high–Mach number jet has been created and characterized (*39*). Here, the initial conditions were a hot (~1 keV), high-velocity (~700 km/s) jet of highly ionized Au plasma, where the radiative cooling effects were large. Perhaps more relevant are experiments under way with the ultrahigh-intensity laser called the Petawatt (*40*). Here, planar targets are irradiated by a laser pulse (10^{20} W/cm^2), producing an expanding high-energy density wave of hot plasma, that is, a "laboratory fireball." The initial plasma temperature is thought to be several megaelectron volts, the plasma is relativistically hot, and electron-positron pairs are created. For the highest intensity shots, electrons have been observed up to energies of 100 MeV, and positron energy spectra have also been recorded (Fig. 3B) (*41*, *42*). Perhaps most interesting in these experiments is the observation of photonuclear reactions. The energetic electrons yield high-energy x-rays through bremsstrahlung (Fig. 3C), which excite the nucleus. The nucleus deexcites by emitting a nucleon or in the case of ^{238}U by fission. These reactions can leave the nucleus in long-lived excited states that can be counted after the fact by γ-ray spectroscopy. The exact laser-plasma dynamics and subsequent plasma fireball evolution are still being worked out. However, what is clear is that plasmas have now been created in the laboratory with a temperature (T) ~1 MeV "thermal" component and a higher energy tail (*40*–*42*). Substantial e^+e^- production and excited nuclear levels have been observed. Hence, aspects of the underlying GRB fireball physics, such as relativistic plasma effects, are becoming accessible in the laboratory.

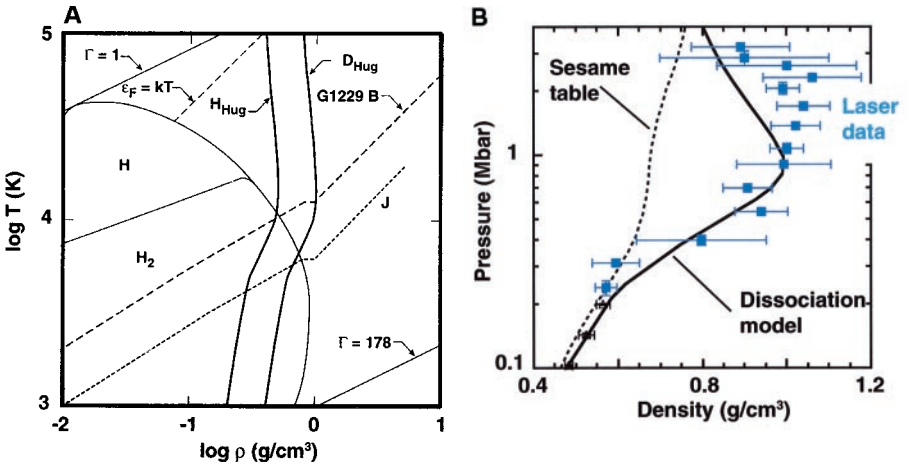

Fig. 4. The phase diagram and EOS experiments relevant to the giant planets and brown dwarfs. (**A**) Theoretical phase diagram of hydrogen [reproduced from (*46*)] relevant to Jupiter (J) and the brown dwarf Gliese 1229B (G1229B). H_{Hug} and D_{Hug} are model hydrogen and deuterium Hugoniots. (**B**) Measured compression (density) versus SW-induced pressure, that is, the measured principle Hugoniot for cryogenic liquid D_2 [reproduced from (*46*)].

Giant Planets and Brown Dwarfs

The "high-stakes tug of war" between quantum mechanical degeneracy pressure and the more familiar gravitational pressure was discussed in the section on SNe. A somewhat more benign environment to consider strong degeneracy effects is in the steady-state interiors of the giant planets such as Saturn and Jupiter and the newly discovered brown dwarfs, (*6*, *43*–*45*) as represented by the phase diagram shown in Fig. 4A (*46*–*48*). Here, because of their lower mass, $M \leq 0.08\ M_\odot$, these bodies never generate sustained thermonuclear fusion as stars, and the degeneracy pressure and strongly coupled effects dominate.

Strongly coupled plasmas are typically characterized by the dimensionless parameter, $\Gamma = (Ze)^2/akT$, where a is a characteristic separation distance between ions, Ze is the ion charge state, and kT is the temperature in units of energy. In plasmas with $\Gamma \ll 1$, thermal effects dominate and the plasma is considered "ideal." When $\Gamma \geq 1$, the Coulomb interactions become an equal player, and the plasma enters the strongly coupled regime, represented by the region to the right and below the $\Gamma = 1$ line in Fig. 4A. When $\Gamma > 178$, the plasma becomes so strongly coupled that the ions freeze solid into a crystal lattice. Also, when the densities are high enough or temperatures low enough that $kT < \varepsilon_F$, where $\varepsilon_F = p_F^2/2m_e = (1/8)(3/\pi)^{2/3}(h^2/m_e)n_i^{2/3} \propto \rho^{2/3}$ is the Fermi energy (p_F is the Fermi pressure and n_i is the ion number density), the plasma is called degenerate, and is represented by the region to the right and below the $\varepsilon_F = kT$ line (Fig. 4A). Here, electron degeneracy pressure becomes a major part of the total pressure. The isentropes for Jupiter and the brown dwarf Gliese 1229B (*45*) (Fig. 4A) indicate that these bodies,

which are made up predominantly of H and He, are both strongly coupled and highly degenerate. Hence, the internal structure, $\rho(r)$, $T(r)$, and to some extent the external magnetic fields of the giant planets and brown dwarfs are determined by the EOS of degenerate hydrogen and helium at high pressure, $p = 1$ to 100 Mbar. The EOS of strongly coupled, degenerate plasma, however, is notoriously difficult to calculate from first-principles theories, because of the complexity of including quantum mechanical effects into classical thermodynamic theories. Experiments in this parameter regime are a vital component in efforts to improve our understanding of Jupiter, the other giant planets, and brown dwarfs.

The EOS of a material can be determined by measuring its response to a known applied pressure. Measurements of the EOS of cryogenic deuterium, D (an isotope of hydrogen), at applied pressures ranging from 220 kbar to 3.4 Mbar have been made on the Nova laser (*46*–*48*). In these experiments, the transition of hydrogen from a molecular fluid insulator phase to a monatomic metallic phase was unambiguously observed. A departure from the standard theoretical EOS models for hydrogen was found in the compressibility of D_2 in this regime (Fig. 4B). The results were consistent with a model that included the potential energy sink caused by molecular dissociation ($D_2 \rightarrow D + D$). These results, together with extensive results from gas-gun experiments at lower pressure (*49*, *50*), have implications for the composition and dynamics of the outer layers of Jupiter, the other giant planets, and brown dwarfs.

The pressure and temperature in the mantle of Jupiter near the surface are in the range of 1 to 3 Mbar and a fraction of an electron volt. Deeper in the interior, the pressure and temperature increase, rising to 40 Mbar and a couple of electron volts at the center (*51, 52*). Near the surface, hydrogen exists as the molecule H_2, but dissociates to H + H and ionizes deeper in the mantle. This transition of hydrogen from insulator to conductor is important, because conducting H in the convective zone is thought to create the 10- to 15-Gauss magnetic field of Jupiter. One of the fundamental open questions about the interior of Jupiter is whether there is a sharp boundary, a plasma phase transition (PPT), between a molecular hydrogen mantle and a monatomic hydrogen core at a radius of ~0.75 jovian radius (R_J) and pressure of 3 Mbar. The regimes accessed by the laser and gas-gun experiments represented on Fig. 4B span this critical transition from mantle to core of Jupiter and suggest that a sharp discontinuity between molecular (mantle of Jupiter) to monatomic (core of Jupiter) hydrogen does not exist. The experiments (*46*–*48*, *51, 52*) suggest that on the jovian isentrope molecular hydrogen probably begins to dissociate at 400 kbar and dissociation continues smoothly to completion at ~3 Mbar, with metallization occurring right in the middle of this region at ~1.4 Mbar and ~4000 K. It is possible (*52*) that currents near the surface of Jupiter, at radii out to 0.95 R_J contribute to the surface magnetic field, whereas previously it was thought that the magnetic field was formed deeper in the interior at ~0.75 R_J.

References and Notes

1. W. D. Arnett, J. N. Bahcall, R. P. Kirshner, S. E. Woosley, *Annu. Rev. Astron. Astrophys.* **27**, 629 (1989).
2. W. Hillebrandt and P. Höflich, *Rep. Prog. Phys.* **52**, 1421 (1989).
3. D. Arnett, *Supernovae and Nucleosynthesis* (Princeton Univ. Press, Princeton, NJ, 1996).
4. H. Bethe, *Rev. Mod. Phys.* **62**, 801 (1990).
5. S. Woosley and T. Weaver, *Sci. Am.* **261**, 32 (August 1989).
6. H. M. Van Horn, *Science* **252**, 384 (1991).
7. D. Arnett, in preparation.
8. B. P. Schmidt *et al.*, *Astrophys. J.* **395**, 366 (1992); *ibid.* **432**, 42 (1994).
9. R.G. Eastman *et al.*, *ibid.* **466**, 911 (1996); *ibid.*, **430**, 300 (1994).
10. D. Branch *et al.*, *Phys. Plasmas* **4**, 2016 (1997).
11. C. A. Iglesias and F. J. Rogers, *Astrophys. J.* **464**, 943 (1996).
12. C. Chenais-Popovics, in preparation.
13. J. Wark *et al.*, *Phys. Plasmas* **4**, 2004 (1997).
14. E. Muller, B. Fryxell, D. Arnett, *Astron. Astrophys.* **251**, 505 (1991).
15. B. Fryxell, E. Muller, D. Arnett, *Astrophys. J.* **367**, 619 (1991).
16. J. Kane *et al.*, *ibid.* **478**, L75 (1997); J. Kane *et al.*, *Phys. Plasmas* **6**, 2065 (1999).
17. B. A. Remington *et al.*, *Phys. Plasmas* **4**, 1994 (1997).
18. D. D. Ryutov *et al.*, *Astrophys. J.*, in press.
19. U. Hwang, J. P. Hughes, R. Petre, *ibid. J.* **497**, 833 (1998); P. F. Velazquez *et al.*, *Astron. Astrophys.* **344**, 1060 (1998).
20. K. J. Borkowski and A. E. Szymkowiak, *Astrophys. J.* 477, L49 (1997); R. Braun, *Astron. Astrophys.* **171**, 233 (1987); E. Dwek, *Astrophys. J.* **322**, 812 (1987).
21. N. A. Levenson *et al.*, *Astrophys. J. Suppl.* **118**, 541 (1998); *Astrophys. J.* **484**, 304 (1997); *ibid.*, 468, 323 (1996); J. J. Hester *et al.*, *Astrophys. J.* **420**, 721 (1994); R. A. Resen *et al.*, *Astron. J.* **104**, 719 (1992).
22. J. C. Raymond, W. P. Blair, K. S. Long, *Astrophys. J.* **454**, L31 (1995); P. F. Winkler and K. S. Long, *ibid.* **486**, L137 (1997); *ibid.* **491**, 829 (1997).
23. J. Hester *et al.*, *ibid.* **456**, 225 (1996).
24. E. Michael, R. McCray, K. J. Borkowski, C. S. J. Pun, G. Sonneborn, *ibid.* **492**, L143 (1998).
25. K. J. Borkowski, J. M. Blondin, R. McCray, *ibid.* **477**, 281 (1997).
26. _____, *ibid.* **476**, L31 (1997).
27. R. P. Drake *et al.*, *Astrophys. J. Lett.* **500**, L157 (1998).
28. R. P. Drake *et al.*, *Phys. Rev. Lett.* **81**, 2068 (1998).
29. J. Kane, R. P. Drake, B. A. Remington, *Astrophys. J.* **511**, 335 (1999).
30. R. A. Chevalier, *ibid.* **258**, 790 (1982).
31. R. I. Klein *et al.*, in preparation.
32. R. Klein *et al.*, *Astrophys. J.* **420**, 213 (1994).
33. T. Piran, in *Unsolved Problems in Astrophysics*, J. N. Bahcall and J. P. Ostriker, Eds. (Princeton Univ. Press, Princeton, NJ, 1997), pp. 343–369.
34. G. J. Fishman and C. A. Megan, *Annu. Rev. Astron. Astrophys.* **33**, 415 (1995).
35. E. Waxman, *Astrophys. J.* **489**, L33 (1997).
36. _____, in preparation.
37. J. H. Krolick and E. A. Pier, *Astrophys. J.* **373**, 227 (1991).
38. E. Liang, M. Kusunose, I. A. Smith, A. Crider, *ibid.* **479**, L35 (1997); E. Liang and V. Kargatis, *Nature* **381**, 49 (1996).
39. D. Farley *et al.*, in preparation.
40. M. H. Key *et al.*, *Phys. Plasmas* **5**, 1966 (1998).
41. T. Cowan *et al.*, in *Proceedings of XXIV ECLIM, Lasers Particle Beams*, in press.
42. T. Cowan *et al.*, in preparation.
43. W. B. Hubbard *et al.*, *Phys. Plasmas* **4**, 2011 (1997).
44. D. Saumon *et al.*, *Phys. Rev. Lett.* **76**, 1240 (1996); *Astrophys. J.* **460**, 993 (1996).
45. T. Nakajima *et al.*, *Nature* **378**, 463 (1995); B. R. Oppenheimer *et al.*, *Science* **270**, 1478 (1995).
46. G. W. Collins *et al.*, *Science* **281**, 1178 (1998).
47. G. W. Collins *et al.*, *Phys. Plasmas* **5**, 1864 (1998).
48. L. B. Da-Silva *et al.*, *Phys. Rev. Lett.* **78**, 483-6 (1997).
49. S. T. Weir, A. C. Mitchell, W. J. Nellis, *Phys. Rev. Lett.* **76**, 1860 (1996).
50. N. C. Holmes, M. Ross, W. J. Nellis, *Phys. Rev. B* **52**, 15835 (1995).
51. W. J. Nellis, M. Ross, N. C. Holmes, *Science* **269**, 1249 (1995).
52. W. J. Nellis, S. T. Weir, A. C. Mitchell, *ibid.* **273**, 936 (1996).
53. J. Glanz, *ibid.* **276**, 351 (1997).

54. The work reviewed here was presented at a workshop supported under the auspices of the U.S. Department of Energy by the Lawrence Livermore National Laboratory under contract number W-7405-ENG-48.